



# Coupled Hydraulic-Mechanical Experimental System for Evaluating Dynamic Mechanical and Transport Behaviors of Deep Rocks

R. Chen<sup>1,2</sup> · G. Zhao<sup>3</sup> · Y. Xu<sup>2</sup> · W. Yao<sup>4</sup> · W. Yao<sup>2</sup> · K. Xia<sup>5</sup>

Received: 26 June 2023 / Accepted: 21 March 2024 / Published online: 18 April 2024  
© Society for Experimental Mechanics 2024

## Abstract

**Background** The dynamic mechanical properties and permeability evolution of deep rocks under coupled osmotic-mechanical conditions are vital for evaluating the stability of surrounding rock in deep rock engineering and further improving deep mining efficiency. However, there is currently no valid experimental system to measure both the dynamic mechanical response and the permeability evolution of deep rocks.

**Objective** In this study, a novel experimental system is developed for determining dynamic compressive properties and permeability evolution of deep rocks subjected to coupled differential pore pressure and confinement.

**Methods** The experimental system is composed of a dynamic loading system, an in-situ stress system, a differential pore pressure system, and a data acquisition system. The differential pore pressure system is introduced in the dynamic loading system, and the validation of the proposed system is verified by checking the stress wave propagation in the bars and the dynamic force balance on the two loading ends of specimens. It indicates that the differential pore pressure device added to the dynamic loading system barely influences the measurement of the dynamic behaviors of rocks. A homogenous green sandstone (GS) is employed to verify the feasibility and reliability of the proposed system. Dynamic compressive strength, permeability evolution, and failure mode of GS under cyclic dynamic impact loading in combination with coupled osmotic-confining pressure are explored using the proposed system.

**Results** The stress–strain curves change with the increase of impact number, and the cyclic impacts deteriorate the dynamic compressive strength of GS. The permeability of GS first increases and then decreases with the impact number. The differential pore pressure enhanced the permeability of GS under the same impact cycle. The main fracture mode of the GS specimen is mainly compressive-shear fracture in combination with a tensile fracture in the middle of the specimen due to the coupling effect of the reflected stress wave and the osmotic-confining pressure.

**Conclusions** The proposed experimental system is valid and effective to measure and observe the dynamic compressive behaviors and permeability evolution of rocks under coupled osmotic-mechanical conditions.

**Keywords** Cyclic impact · Deep rock, Permeability · Compressive strength, Differential pore pressure · Confinement

---

K. Xia is a member of SEM.

---

✉ W. Yao  
yaow@tju.edu.cn

<sup>1</sup> College of Sciences, National University of Defense Technology, Changsha 410073, China

<sup>2</sup> State Key Laboratory of Hydraulic Engineering Intelligent Construction and Operation, School of Civil Engineering, Tianjin University, Tianjin 300072, China

<sup>3</sup> Yalong River Hydropower Development Company, Ltd., Chengdu 610065, Sichuan, China

<sup>4</sup> China National Coal Group Corporation, 1 Huangsi St., Chaoyang District, Beijing 100120, China

<sup>5</sup> Institute of Geosafety, China University of Geosciences (Beijing), Beijing 100083, China

## Introduction

Deep rock engineering (e.g., the exploitation of the deep resources and energy) is inevitably involved in the assessment of the stability of deep rocks, which are generally subjected to a complex geological environment with high in-situ stress, high differential pore pressure, high temperature, and dynamic disturbances caused by operational blasting and earthquakes [1–4], etc. Mitigation of geological hazards in deep rock engineering is challenging as the deep rocks experience the extremely complex geological environment mentioned above. Especially, geological hazards (such as water inrush, water gushing, rockburst, coal and gas outburst,

etc.) are prone to occur in deep rock with high differential pore pressure when the dynamic disturbances induced by the fault activation and operational blasting are exerted on deep rocks, severely affecting project progress and personnel safety. Therefore, the failure behaviors of deep rocks with differential pore pressure triggered by dynamic disturbances have attracted great attention worldwide in the deep rock engineering community. Understanding the dynamic mechanical and transport behaviors of deep rocks is essential for revealing the failure mechanism of deep rocks for the safe and efficient exploitation of deep resources and energy.

Some studies have been conducted by scholars on the dynamic mechanical behaviors of rocks with water saturation [5–10]. Generally, the dynamic compressive strength of water-saturated rocks is generally lower than that of dry rocks. However, there is an exceptional phenomenon, i.e., when the strain rate exceeds a certain threshold ( $180 \text{ s}^{-1}$ ), the dynamic compressive strength of water-saturated rocks may be higher than that of dry rocks [11]. The enhancement mechanisms of water on the dynamic mechanical properties of rocks can be mainly categorized as follows: (1) Inertia effect increased by saturated water (The inertia effect increases with the rock mass and the mass of the water-saturated specimen is higher than that of the dry specimen with the same volume due to the water in the rock specimen.) [5]; (2) Local damage of rocks reduced by saturated water (Stress waves reflect off the primary fissure surfaces of dry rocks, resulting in localized damage within the rock, which reduces the rock strength. However, when stress waves propagate within water-saturated rocks, the body of water in the fissure can act as a wave propagation medium, which reduces wave reflections off the crack surfaces and reduces localized damage within the rock, thereby increasing the rock strength.) [5]; (3) Plate effect caused by water surface tension [6, 7]; (4) Stefan effect caused by water viscosity [6, 7] and Newtonian internal friction effect [11]. Furthermore, previous studies have shown that the presence of water has a significant influence on the fracture patterns and energy distribution of rocks under dynamic loading [8–10]. As the increase of the water content in rocks, intergranular fractures are more likely to occur in rocks because water pressure has a certain weakening effect on the bonding strength between crystal particles. Hence, the proportion of large fragments decreases while the proportion of small fragments increases. Meanwhile, the effect of water on the total dissipated energy of rocks is not significant (The total dissipated energy was defined as the shadow area under the stress–strain curve during the whole loading period.). However, the dissipated energy of water-saturated rocks in the pre-peak stress region (The pre-peak dissipated energy was obtained by using the shadow area under the stress–strain curve before the peak stress.) is smaller than

that of dry rocks, and as the water content increases, the dissipated energy in the pre-peak stress region decreases. Similarly, the dissipated energy of water-saturated rocks in the post-peak stress region is greater than that of dry rocks, and as the water content increases, the dissipated energy in the post-peak stress region increases [8–10]. The low energy of water-saturated rocks in the pre-peak stress region can be explained by the increase in pore water pressure caused by rock compression during pre-peak loading, which promotes crack propagation and energy dissipation. The energy of water-saturated rocks in the post-peak stress region is relatively high, which can be understood as the expansion of compressed pores in the rock during the post-peak unloading stage, requiring more energy to overcome the stress caused by the viscosity of water [8–10].

Although the dynamic mechanical properties of rocks with different water contents have been investigated in previous studies, there is no osmotic or pore pressure in rocks. In true deep rock engineering projects, the pore water in rock masses experiences a certain degree of differential pore pressure due to gravity and other factors. Therefore, it is essential for true deep rock engineering to investigate the dynamic mechanical characteristics of rocks under differential pore pressure. Zhou et al. [12] created a prefabricated single crack and water injection hole inside the rock specimen to introduce water pressure in the crack and then conducted dynamic impact tests on the specimens using a split Hopkinson pressure bar (SHPB). However, this method is only applicable to prefabricated specimens. Wang et al. [13] developed an experimental device that can provide both differential pore pressure and confining pressure on the specimen based on the SHPB system. The coal specimens under both differential pore pressure and confining pressure were tested under dynamic loading. The principle of this device is that the differential pore pressure exerted on the rock specimen was induced by the confining pressure. Both the pore pressure and the confining pressure of the rock specimen are achieved by the water. When the confining pressure is applied by the water, water permeates into the rock specimen through the pore space and then exerts the pore pressure. The confining pressure and the pore pressure are identical. Although this design can achieve the pore pressure on the rock specimen, it cannot provide separately the confining pressure and the pore pressure when the pore pressure is not equal to the confining pressure. The confining pressure and the pore pressure are not consistent in practice, the applicability of this device thus is limited. Zhao et al. [14] developed a dynamic rock testing system in combination with the static triaxial loading device and the pore pressure loading device. The triaxial stress and the pore pressure can be applied separately in this system and the principle and feasibility of this system can be found in

the literature. However, this system cannot exert differential pore pressure on the rock specimen. As mentioned above, few attempts have yet been made to investigate the dynamic behaviors of rocks under both differential pore pressure and triaxial stress state.

It is well known that rock masses are commonly subjected to high-strain rate cyclic impacts generated by operational blasting or earthquake. Therefore, it is necessary for true deep rock engineering to study the evolution of permeability in rocks under high-strain rate cyclic impacts. Some studies have been performed using the SHPB to achieve multiple-impact tests on rocks and the influence of cyclic impacts on the rock permeability has been investigated [15–17]. The results indicated that at lower impact velocities, rock pores are first compressed and closed by the impact, decreasing porosity and permeability. As the number of impacts increases, pores are expanded, and porosity increases. During the cyclic impact process, the number of large- and small-sized pores decreases while medium-sized pores increase, resulting in an increase in pore connection and the permeability of rocks according to the evolution of rock pores characterized by nuclear magnetic resonance images. At higher impact velocities, the rock is destroyed upon the first impact, resulting in a significant increase in permeability. However, the limitation of these studies is that the permeability of rocks was measured after the cyclic impacts are totally completed and thus the evolution of the permeability cannot be observed during the cyclic impacts.

Although many studies have been performed to understand the dynamic mechanical properties of water-saturated rocks and rocks with pore pressure and some investigations have focused on the permeability of rocks after multiple impacts, few attempts have yet been made to develop an experimental system for measuring the dynamic properties and the permeability evolution of rocks under both differential pore pressures and cyclic impacts. Therefore, it is necessary to develop a rock dynamic testing system that can simulate both the differential pore pressure and the dynamic loads in deep rocks in practice and to further explore the influence of the differential pore pressure on the dynamic mechanical responses and permeability evolution of deep rocks. In this study, a triaxial dynamic rock testing device with a differential pore pressure system is first proposed in detail to quantify the dynamic compressive behaviors of rocks subjected to triaxial stress and differential pore pressure. The wave propagation on the proposed testing device was validated to confirm its feasibility and reliability. With the dynamic stress balance being achieved, dynamic compression experiments under a static triaxial stress state and fourteen impact cycles in combination with various differential pore pressures were conducted to evaluate the dynamic compressive characteristics and permeability evolution of deep rocks, based on which the dynamic failure mechanism of deep rocks under the bidirectional

effects of differential pore pressure and multiply impacts was subsequently revealed.

## Experimental Methodology

### Triaxial Dynamic Rock Testing Apparatus with Differential Pore Pressure System

To investigate the effect of differential pore pressure on the dynamic mechanical properties and permeability evolution of deep rocks, a differential pore pressure system was introduced in the triaxial SHPB system. As illustrated in Fig. 1, this system is mainly composed of a 50 mm conventional SHPB system, an in-situ stress system, a differential pore pressure system, and a data acquisition system. The bars are made of high strength maraging steel with a diameter of 50 mm. The lengths of the striker, the incident bar, and the transmitted bar are 700 mm, 3000 mm, and 1800 mm, respectively [18]. To ensure that the rock specimen was under single dynamic loading for each impact cycle, a momentum trap technique was employed in this work to achieve a single dynamic compressive pulse on the rock specimen. The key idea of the momentum trap technique is to absorb the first reflection by a big mass that can be considered rigid due to its large impedance as compared to the incident bar. An appropriate gap between the flange and the rigid mass is selected [19]. Hence, the flange can be in contact with the big mass when the reflection wave arrives at the impact end of the incident bar. With the interaction between the flange and the big mass, the reflected compressive wave is transferred into tension. This tensile pulse prevents compression on the rock specimen. More details of the momentum trap can be found in previous studies [19–21].

The rock specimen is subjected to both in-situ stress and differential pore pressure. The schematic of the in-situ stress device and the differential pore pressure device is shown in Fig. 1. To simulate the in-situ stress environment within which the deep rocks experience, the in-situ stress system is composed of a cylinder (i.e., Cylinder 1 that provides a confining pressure for the rock specimen) and a pressure chamber (i.e., Cylinder 2 that provides an axial pre-load for the rock specimen), respectively (Fig. 1). Both the axial pre-load and the confining pressure can reach up to 100 MPa. This is an active and stable triaxial loading system, where the confining pressure and the axial pre-load can be independently servo controlled [22]. Hence, the confining pressure can be different from the axial pre-load in the experiment. In addition, as shown in Fig. 1, the differential pore pressure system consists of an electro-hydraulic servo loading device, a guide bar and a modified incident bar with two symmetrical pinholes and a circular diversion groove, two sealing flanges, a vacuum pump, metal water pipes, and valves. All

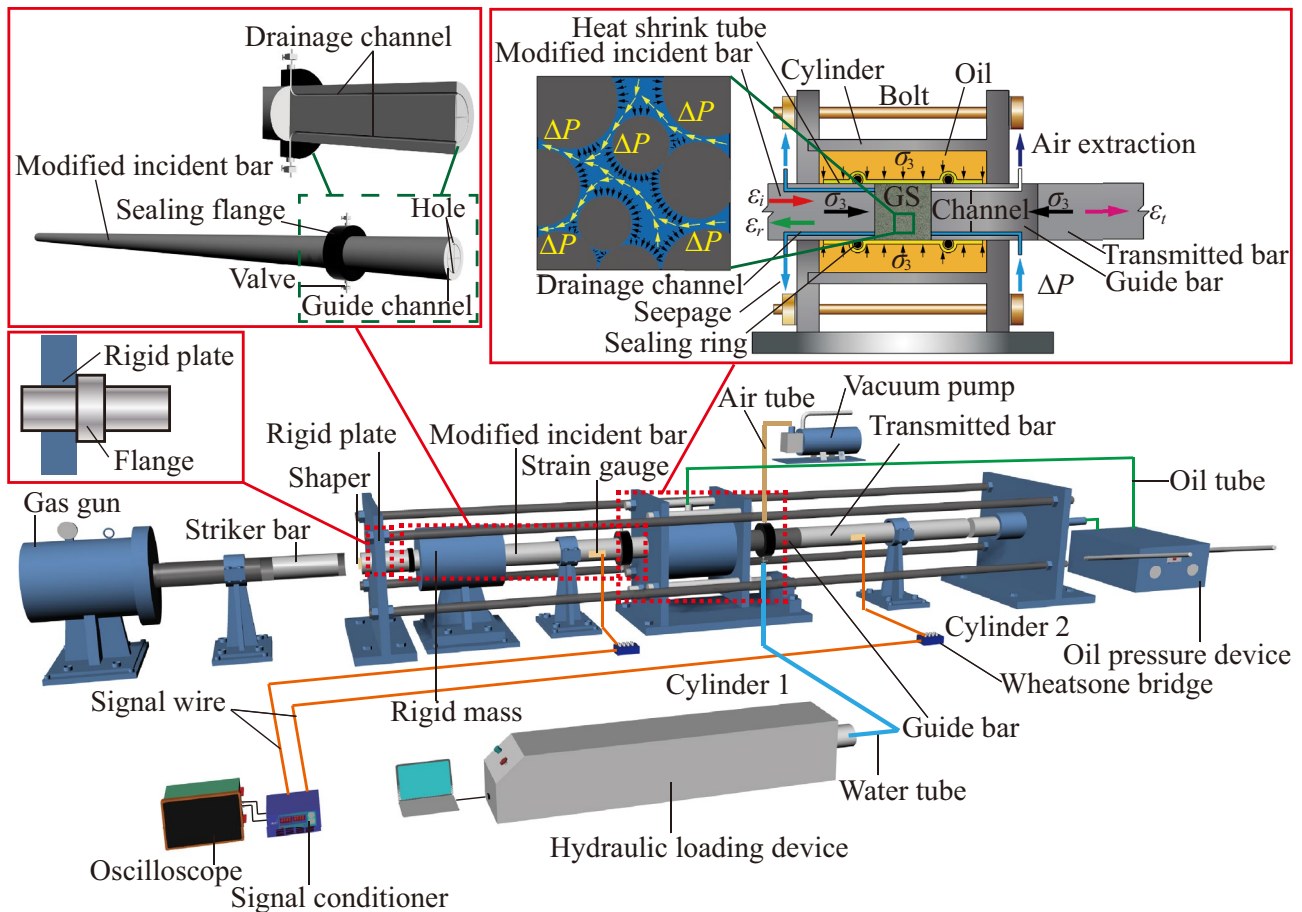


**Fig. 1** The triaxial SHPB system with the differential pore pressure system

these components can be assembled into the triaxial SHPB testing system. The modified incident bar and the guide bar are essential components for differential pore pressure loading and stress wave transmission, and thus the structures of the incident bar and the guide bar are specially designed. The guide bar passes through the confining cylinder and is located between the incident bar and the transmission bar. The material of the guide bar is the same as that of the incident bar and the transmission bar, which can avoid the stress wave reflection caused by the inconsistent wave impedance. Besides, the rock specimen is sandwiched between these two bars and the ends of these two bars with the grooves are attached to the rock specimen. At the ends of the modified incident bar and the guide bar which contact with the rock specimen, diversion grooves in the shape of a circle and cross are made, aiming to uniformly disperse the water pressure on two ends of the rock specimen. In addition, two pinholes with a diameter of 1 mm are drilled along the axis of the guide bar. One of the pinholes in the guide bar is employed for extracting excess air from rock pores and the heat shrink tube. The other one serves as the fluid transport channel (i.e., differential pore pressure loading channel),

through which the high-pressure water from the servo water pressure loading device can easily access the rock specimen and the water pressure can act on one end of the rock specimen. This fluid transport channel is connected to the water pressure loading device through the sealing flange and the metal water pipe during the experiment. With the design of two pinholes, the air can be easily discharged to ensure that the servo water pressure loading device is filled with water.

To allow the water to permeate through the rock specimen, two pinholes with a diameter of 1 mm were drilled along the axis of the incident bar and diversion grooves are manufactured on the end of the incident bar, as shown in Fig. 1. Similar to the guide bar, the diversion grooves are contacted to the ambient atmosphere through two pinholes (Fig. 1). These two pinholes in the incident bar are used as the drainage channels, with which the water permeated through the rock specimen discharges to the air and the water pressure on this end of the rock specimen equals the atmospheric pressure. The electrohydraulic servo water pressure loading device is controlled by a computer and can perform servo control in multiple modes, e.g., a constant water pressure mode and a constant flow rate mode with a maximum pressure of 40 MPa.

**Table 1** Basic physical and mechanical properties of GS

Density (kg/m <sup>3</sup> )	P-wave velocity (m/s)	Uniaxial compressive strength (MPa)	Brazilian tensile strength (MPa)	Young's modulus (GPa)	Poisson's ratio	Porosity (%)
2330	3500	40.0	5.4	8.5	0.3	12

The data acquisition system mainly includes a water pressure data acquisition system and a dynamic loading data acquisition system. Several real-time parameters (including the water pressure, the displacement of the hydraulic press lever, and the flow rate) can be recorded by the water pressure data acquisition system through the water pressure sensor and LVDT (Linear Variable Differential Transformer). The water pressure data can be collected by a computer that also controls the water pressure machine. The dynamic loading data acquisition system is mainly composed of two pairs of strain gauges, a Wheatstone bridge, a signal conditioner, and a digital oscilloscope. Two pairs of strain gauges are stuck at symmetrical positions on the bars respectively to capture the strain signals induced by the incident/reflected wave ( $\epsilon_i/\epsilon_r$ ) on the incident bar and the transmitted wave ( $\epsilon_t$ ) on the transmitted bar. The strain signals are amplified by Wheatstone bridge circuits and the signal conditioner, and subsequently recorded and stored by the digital oscilloscope.

### Specimen Preparation

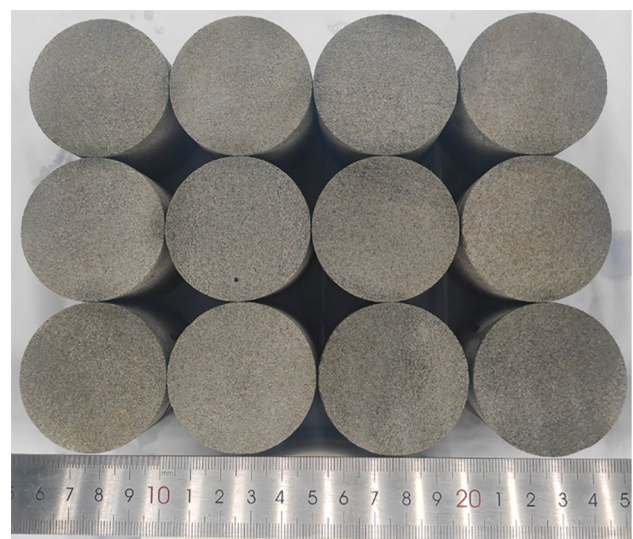
A green sandstone (GS), a typical homogenous sedimentary rock, from Sichuan Province, China was used in this study. The mineral composition of GS is mainly composed of quartz (30.4%), plagioclase (27.17%), iron magnesium oxide (12.15%), potassium feldspar (10.31%), and other minerals (19.97%). The size of minerals is in the range of 10~200  $\mu\text{m}$ .

According to the requirements of rock specimens for determining the static and dynamic compressive strength of rocks recommended by the International Society for Rock Mechanics and Rock Engineering (ISRM) [23, 24], the aspect ratio of rock specimen in this study is 1:1 and the diameter of the rock specimen is 50 mm. The cores of 50 mm in diameter were first drilled from the same rock block along the same orientation and then sliced into cylinders with the nominal length of 50 mm. The ends of the rock specimen were carefully polished with a flatness and perpendicularity less than 0.02 mm and 0.06° respectively, and its straightness should be controlled within 0.02 mm throughout the entire length. The basic physical and mechanical properties of GS are given in Table 1 [25]. Prior to the dynamic experiment, GS specimens (as shown in Fig. 2) were fully saturated by using the vacuum saturation method [14]. It should be noted that distilled water that has very slow kinetics in silicate rocks was used in this study, limiting the impact of reactions. This may affect the experimental results.

### Experimental Procedure

Before the dynamic experiment, the fully saturated GS specimen was clamped between the incident bar and the guide bar by a small axial pressure, and then two sealing rings were placed on the sides of the incident bar and the guide bar to prevent the leakage of water from the rock/bar interfaces (Fig. 1). It is noted that there is no lubricant between the bars and the specimen to ensure that the water can smoothly flow through the GS specimen. This is different from that in the traditional SHPB experiment, in which the interfaces between the specimen and the bars should be fully lubricated to avoid the end friction effect. Meanwhile, to prevent water from flowing out of the gap between the specimen and the heat shrink tube, lubricant (i.e., vacuum grease) was applied on the side of the specimen and the bars worked as a water barrier. Thereafter, the heat shrink tube wrapped up the rock specimen and two rings on bars and was contracted using the heat gun to remove the air cavities in the heat shrink tube, tightly wrapping around the GS specimen and the side of bars and sealing rings, as shown in Fig. 1. In this way, the rock specimen can be completely sealed by the heat shrink tube and entirely isolated from the surrounding hydraulic oil during the dynamic loading.

Afterward, the cylinder (Cylinder 1) providing the confining pressure was installed and locked with four high-strength

**Fig. 2** The fully saturated green sandstone specimens

bolts and a connection bar was placed at the end of the transmitted bar to transmit the axial pressure from the Cylinder 2. The hydraulic oil was used in these two cylinders to provide the confining and axial pressure [26, 27]. The axial pressure and confining pressure were exerted slowly (i.e., 0.1 MPa/s) and uniformly up to a desired value and kept stable to mimic the stress environment of deep rocks. During the loading procedure of the confining and axial pressure, it is noted that the axial pressure should always be slightly greater than the confining pressure to prevent excessive confining pressure from offsetting the axial pressure, causing the detachment of the specimen.

Differential pore pressure was applied to the GS specimen by using the servo water pressure loading device. The response time of the servo-controlled water loading device is 0.02 s (i.e., 50 Hz). The length of the pipeline between the specimen and the servo-controlled water loading device is 1 m. This water loading device is controlled by a servo motor. The encoder resolution of the servo motor is 10000, which means that one pulse signal rotates the motor by 1/10000 degrees. This accuracy of this servo motor can achieve the precise control of water pressure or flow rate. In addition, the servo-controlled water loading device cannot overcompensate the pore pressure during the dynamic loading process because the dynamic loading process is completed within several microseconds and the response time of this servo-controlled water loading device is much longer than the period of dynamic loading process. Meanwhile, it is unnecessary to overcompensate the pore pressure during the dynamic loading process since the permeability of the rock specimen after the dynamic loading is measured in this study. Moreover, the air in the sealed tube and the pipeline was extracted by a vacuum pump after keeping the water inlet channel and the drainage valves closed (Fig. 1). Subsequently, after the completion of the vacuum, the vacuum valve was closed, and the drainage valve and the water inlet channel were opened. Using the servo water pressure loading device, the space around the rock specimen was first filled with the distilled water, and then the water was slowly injected into the pores of the GS specimen from one specimen end. Since the drainage channels in the incident bar are open, the distilled water permeated to the other end of the specimen along the axial direction and then was discharged through the water guide groove and drainage channels in the incident bar. It can be seen that the right end of the GS specimen through the drainage channels is always connected to the ambient atmosphere (Fig. 1), and thus the water pressure on this end of the GS specimen is zero. The gradient of differential pore pressure that the specimen withstands is equal to the water pressure ( $P_w$ ) exerted on the left end of the specimen, i.e.,  $\Delta P = P_w - 0$ . It is noteworthy that the differential pore pressure in the specimen should be less than the hydrostatic pressure during the whole experiment. The

process for exerting the water differential pore pressure on the rock specimen can be divided into three stages: (a) The push rod in the servo water pressure loading device was set in a stepwise manner because the water pressure loading is generally stepwise in traditional seepage experiments; (b) The speed of the push rod is significantly slowed down when the water pressure reaches the predetermined value. At this stage, the speed of the push rod remains unstable since water is permeating the rock specimen and the permeation process is relatively unstable. (c) When water droplets appear at the outlet of the drainage channel in the guide bar, it indicates that water completely permeates through the rock specimen. At the same time, the speed of the push rod remains stable and constant (i.e., the push rod is actively driven into the specimen at a constant rate to keep the constant differential pore pressure in the specimen), indicating the permeation process becomes stable. Consequently, the flow rate of water injection in a servo water pressure loading device is equal to the flow rate of permeation.

When the preset differential pore pressure in the rock specimen was achieved and kept stable, the dynamic impact can be conducted. As shown in Fig. 1, the axial pre-load system includes Cylinder 2 and a rigid plate attached to the incident bar with a tiny flange. When the hydraulic pressure in Cylinder 2 is exerted on the transmitted bar, the axial pre-load is applied to the two ends of the specimen because four tie-rods fix the leftward movement of Cylinder 2 and the incident bar. During the dynamic loading process, the incident wave can smoothly propagate along the incident bar since the motion rightward of the flange and the incident bar is not restrained. To keep the differential pore pressure constant during the impact, the velocity of the push rod in the servo water pressure loading device would be changed for a short time and then remain stable again after the impact. The permeability for each impact was calculated when the velocity of the push rod was stable. Following the above steps, the dynamic compression tests can be repeated until the permeability of the GS specimen was stable, or the specimen is no longer capable of bearing dynamic compressive loads. After dynamic experiments, the differential pore pressure was released and the triaxial stresses were then released. It is noteworthy that the pore pressure inside the specimen during the dynamic stress ramp changes with the variation of the dynamic load, and the effect of the dynamic stress ramp on the pore pressure of the specimen is complicated. However, the changes of the pore pressure and permeability of the specimen during the dynamic loading phase is not research objective in this study. The permeability change of the specimen before and after the dynamic loading is our research objective. In such a case, the servo-controlled water loading device can keep the water pressure constant in the drainage channels before and after the dynamic loading phase to ensure the validation of the testing system.

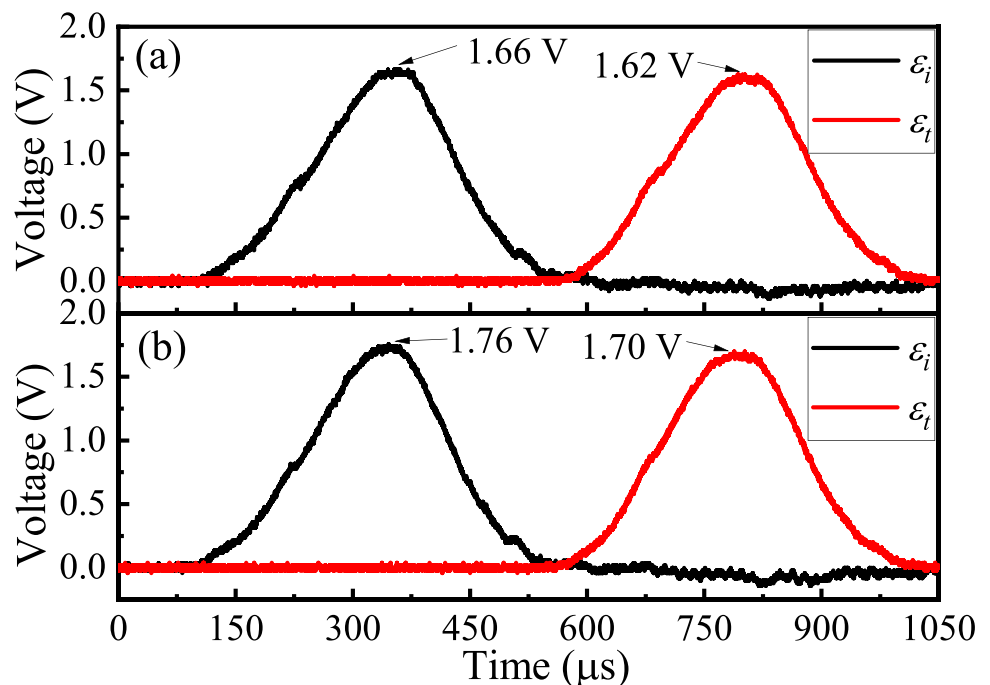
## Validation of Testing System and Data Reduction

### Validation of Dynamic Loading System

In this study, since the special guide bar and the modified incident bar were assembled in the conventional SHPB system [28–30], the one-dimensional stress wave propagation, which is one of the basic requirements of a valid dynamic SHPB test, might be challenged in the proposed system. Hence, the one-dimensional stress wave propagation in the proposed dynamic rock testing system was checked to verify the validation of this improved SHPB system in this study. The stress wave propagation without the specimen between two bars in the conventional SHPB system is shown in Fig. 3a. The stress wave obtained from the incident bar is almost identical to that captured in the transmitted bar, indicating that the one-dimensional stress wave propagation is valid. The same method was used to verify the validation of this improved SHPB system in this study. The stress wave propagation in the improved SHPB system without the specimen is shown in Fig. 3b. When the guide bar was assembled in the conventional SHPB system and the incident bar was replaced by a special incident bar with two drainage channels, the stress wave in the transmitted bar is almost equal to that in the incident bar, demonstrating that the shapes of the stress waves are barely influenced by the guide bar and the amplitudes of stress waves in two bars are very close each other. The

amplitude of the incident wave is 1.76 V, and the amplitude of the transmitted wave is 1.70 V. This loss of the amplitude (about -3.3%) in the stress wave may be caused by the special structure of the incident bar. Meanwhile, the process for checking the validation of the improved SHPB system in this study is the same as that for checking the alignment of the SHPB system in the SHPB research community. In the SHPB testing system, if no reflected wave is generated when the incident bar is in contact with the transmitted bar without any specimen in between, there is a good alignment between the incident and the transmitted bar, and the one-dimensional stress wave propagation is valid. The complete incident pulse in the incident bar should be transmitted into the transmission bar without any reflection, meaning that the transmitted wave is the same as the incident wave. However, slight difference between the incident wave and the transmitted wave may occur due to the error induced by the data acquisition system. Therefore, the difference between these two waves is acceptable by the SHPB research community if this difference is less than 5% [1]. Similarly, this difference (error) between these two waves in this study is mainly induced by the special structure of the incident bar and the transmitted bar, and the error is less than 5%. As a result, the error is tolerable quantitatively. Therefore, it is approved that the improved SHPB system with the guide bar and the special incident bar satisfies the basic principle of one-dimensional wave propagation and is valid to measure the dynamic mechanical and transport behaviors of rocks.

**Fig. 3** Stress wave propagation (a) in a traditional SHPB system and (b) in the triaxial SHPB with the guide bar and the modified incident bar



Based on one-dimensional stress wave propagation, the forces  $F_1$  and  $F_2$  on both ends of the specimen can be written as:

$$F_1(t) = EA(\varepsilon_i(t) + \varepsilon_r(t)), F_2(t) = EA\varepsilon_t(t) \quad (1)$$

where  $E$  and  $A$  are the elastic modulus and cross-sectional area of the bars, respectively;  $\varepsilon_i$ ,  $\varepsilon_r$ , and  $\varepsilon_t$  are the strain history of the incident wave, the reflected wave, and the transmitted wave in the bars, respectively. In addition, the dynamic force balance is an important requirement for a valid dynamic rock test using the SHPB system [24]. The dynamic force balance obtained from a typical experiment using the improved SHPB system is shown in Fig. 4. It can be seen that the forces on two ends of the water-saturated and dry rock specimens can be achieved by using the improved SHPB system, indicating that this testing system with the special guide bar and the modified incident bar is also valid to measure the dynamic behaviors of rocks.

### Determination of Permeability and Dynamic Mechanical Parameters of Rocks

As shown in Fig. 1, the schematic of the differential pore pressure loading system in this study is similar to the principle of the differential pore pressure loading system in a traditional static triaxial loading system [31]. Therefore, the micromechanical seepage model was applied to analyze the permeability of rocks. The nature of seepage in rocks is closely related to the crack configuration inside rocks, which are generally used to construct the micromechanical seepage model. In this study, the rock specimen is a regular cylinder, which is subjected to uniform force and deformation in

the transverse and longitudinal directions, and the direction of seepage can thus be assumed as a single-direction seepage in this study. As a result, the micromechanical seepage model can be simplified. According to the Carman-Kozeny equivalent capillary principle [32], the equivalent pore size of cracks in the micromechanical seepage model can be processed to obtain the equivalent pore size model, as shown in Fig. 5. The volume of the fissure is consistent with the volume of the equivalent pore, and the equivalent pore is a pore with a uniform pore diameter whose length is distributed over the ultimate length of cracks. Based on the micromechanical seepage model, we assumed that the seepage channel in the rock is a circular tubular channel and the water flow through the pores of the rock can be simplified as pipe seepage. Therefore, the water flow state in the rock specimen was determined by estimating the Reynolds number  $Re$  of the water flow in the rock specimen. The Reynolds number of the water flow is calculated by

$$Re = \frac{\rho_w v_w d}{\mu_w} \quad (2)$$

where  $\rho_w = 1000 \text{ kg/m}^3$  is the density of water,  $v_w$  (generally within 26 mm/s) is the velocity of water flow in the rock seepage channel (The velocity here was obtained from the speed of advancement of the push rod),  $d$  (generally within 1 mm) is the diameter of the seepage pipeline,  $\mu_w$  is the dynamic viscosity coefficient of the fluid and equals to  $1.005 \times 10^{-3} \text{ Pa}\cdot\text{s}$  at room temperature. Thus, the Reynolds number of the water flow in rock specimens can be calculated and is about 25.9 in our experiments. Generally, the flow is laminar when the Reynolds number is less than 2100 if the micromechanical seepage model is applied. Hence, it

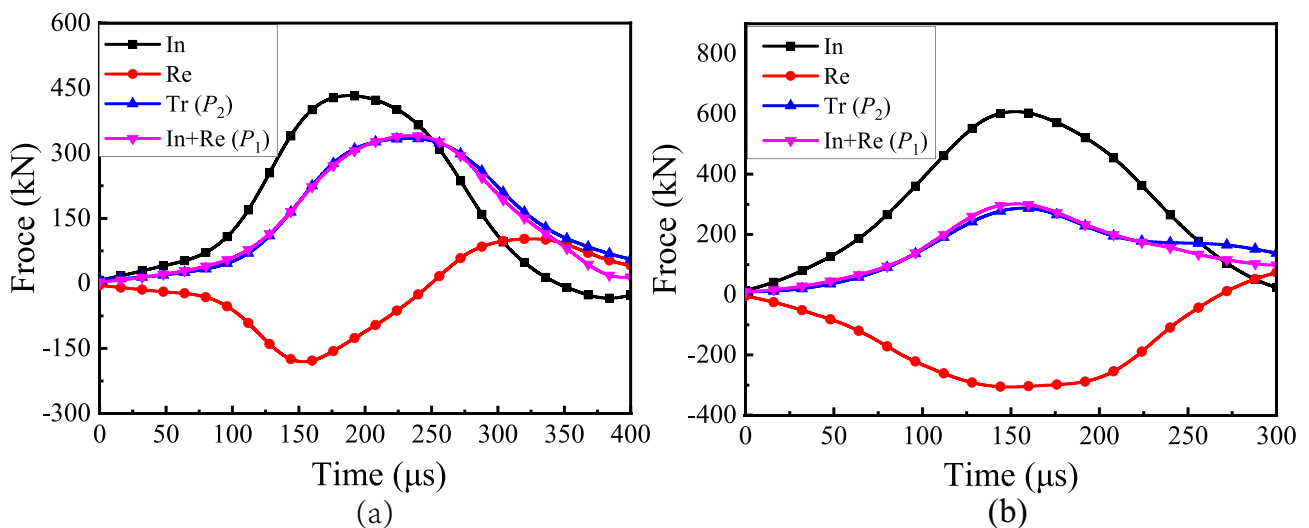
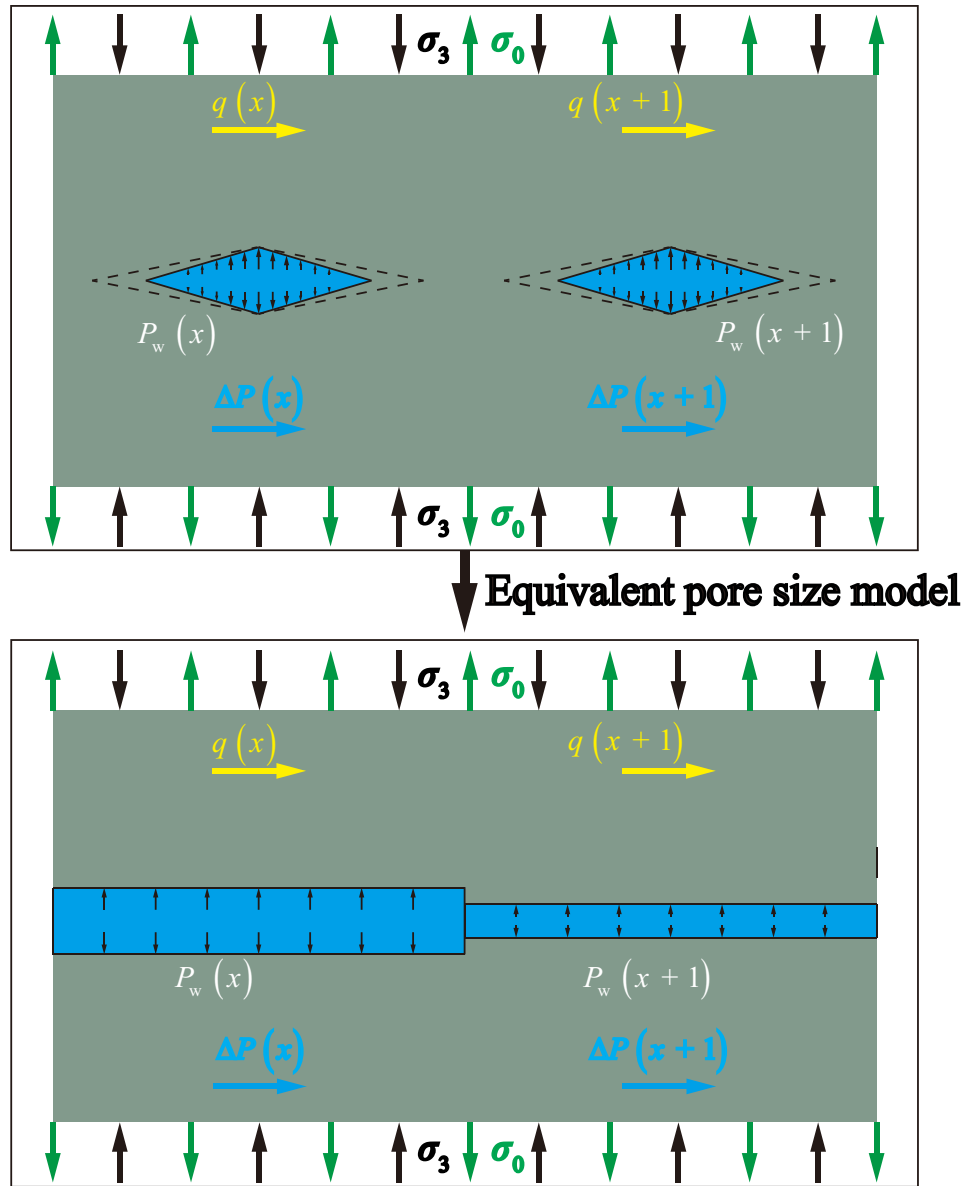


**Fig. 4** Dynamic force balance of (a) the water-saturated GS specimen and (b) the dry GS specimen under the similar loading rate in typical dynamic experiments



**Fig. 5** The equivalent pore size model



is reasonable to assume that the water in the rock specimen remains in a stable laminar state during the testing process, ensuring that Darcy's law is valid for the water flow in the rock specimen in this study. Consequently, the steady-state method can be used to determine the permeability of rock specimens [33]:

$$Q = k_N \frac{\Delta P A_0}{\mu l_0} \quad (3)$$

where  $Q$  is the seepage discharge,  $k_N$  is the permeability of the specimen after the  $N^{\text{th}}$  impact ( $N=0, 1, 2, 3$ ),  $\Delta P$  is the differential pore pressure,  $l_0$  and  $A_0$  are the original length and cross-sectional area of the specimen, respectively. The original length of the specimen is 50 mm, and the

cross-sectional diameter is 50 mm. The water injection flow rate  $q$  of the electro-hydraulic servo water pressure loading device can be determined by

$$q = V_N S \quad (4)$$

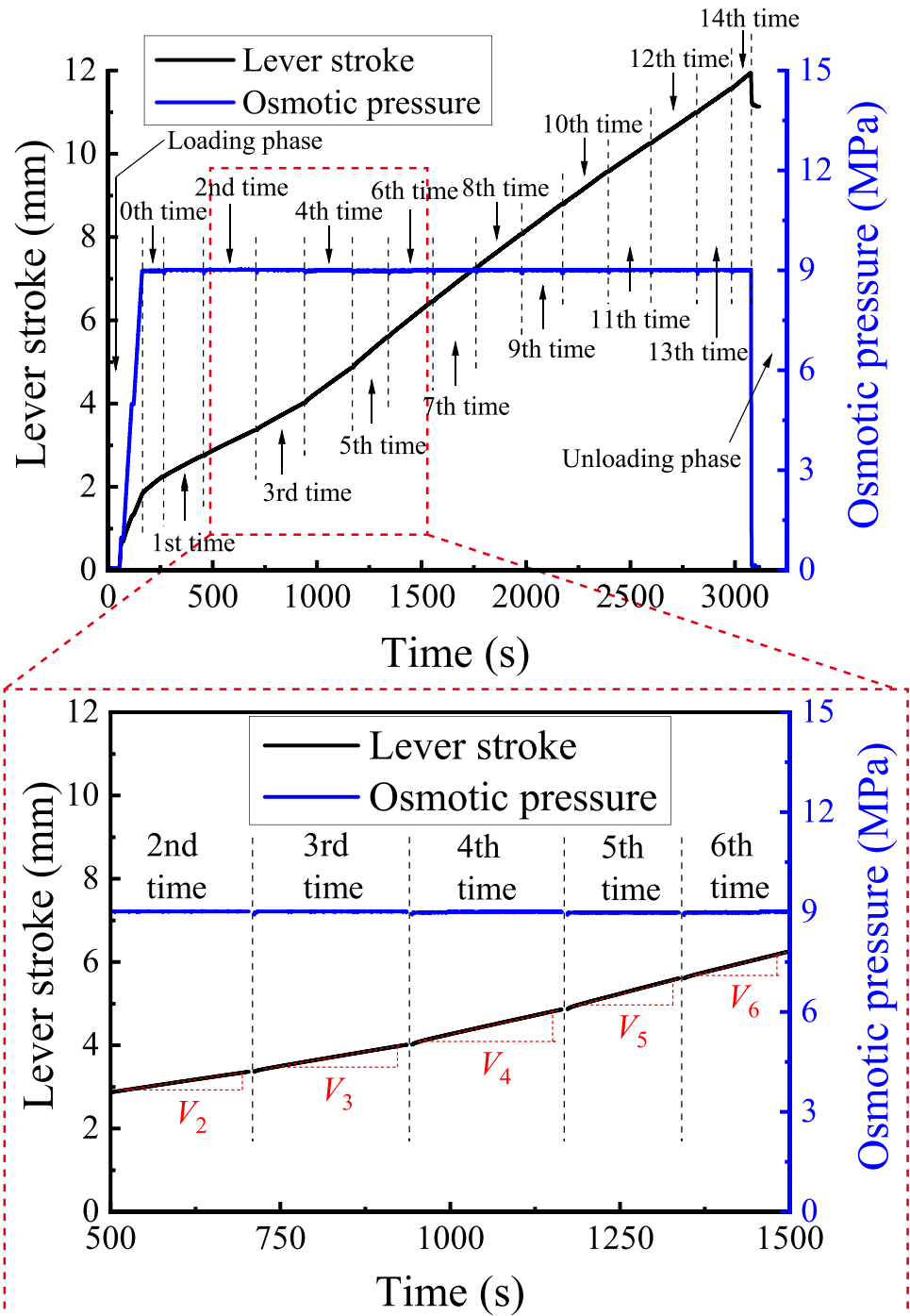
where  $V_N$  is the lever velocity after the  $N^{\text{th}}$  impact, which can be determined by the slope of the lever stroke curve after the seepage stability is reached;  $S=2826 \text{ mm}^2$  is the cross-sectional area of the hydraulic piston of the electro-hydraulic servo water pressure loading device. At a stable seepage process, the water injection flow rate of the hydraulic piston equals the seepage discharge, i.e.,  $Q=q$ . By substituting Eq. (4) into Eq. (3), the formula for calculating the permeability of rock specimens can be obtained

$$k_N = V_N \frac{\mu S l_0}{\Delta P A_0} \quad (5)$$

The unit of  $k_N$  is md and  $1 \text{ md} = 0.987 \times 10^{-9} \text{ mm}^2$ . In addition, the axial pressure on two ends of the specimen is slightly greater than the confining pressure before the dynamic load, and the force balance on the rock specimen can be achieved transiently during the dynamic loading process. Hence, the axial pressure on two ends of the specimen is always larger than the confining pressure during the

dynamic loading, and the ends of bars are always in contact with two ends of the specimen. Consequently, the evolution of the permeability of rock specimens after each impact can be calculated using the obtained lever stroke curve. The lever stroke curve and the corresponding differential pore pressure for each impact in the typical experiment are shown in Fig. 6. It can be seen that the lever velocity can be obtained from the lever stroke curve, and the differential pore pressure for each impact is almost constant during the whole permeation process.

**Fig. 6** Lever stroke and the corresponding differential pore pressure in a typical cyclic impact experiment



When the dynamic forces at both ends of the specimen are balanced, i.e.,  $F_1 = F_2$  or  $\epsilon_1 + \epsilon_r = \epsilon_t$ , the average axial strain  $\epsilon(t)$  and the average stress  $\sigma(t)$  can be obtained by

$$\epsilon(t) = -\frac{2c_0}{l_0} \int_0^t \epsilon_r(\tau) d\tau \tag{6}$$

$$\sigma(t) = \frac{EA}{A_0} \epsilon_t(t) \tag{7}$$

where  $l_0$  and  $A_0$  are the initial length and cross-sectional area of the specimen, respectively. The stress–strain curve of the specimen during the dynamic loading can be obtained from Eqs. (6) and (7). The dynamic strength  $\sigma_{max}$  is defined as the maximum stress value of the stress–strain curve, representing the maximum load that the specimen can bear under a certain loading condition.

### Dynamic Mechanical Characteristics of Rocks Under Cyclic Impact

#### Dynamic Stress–strain Curves

To systematically investigate the permeability evolution due to rock damage induced by the cyclic impact, the rock specimen for each experiment was under 14 cyclic impacts with the constant velocity of the striker. All experiments are

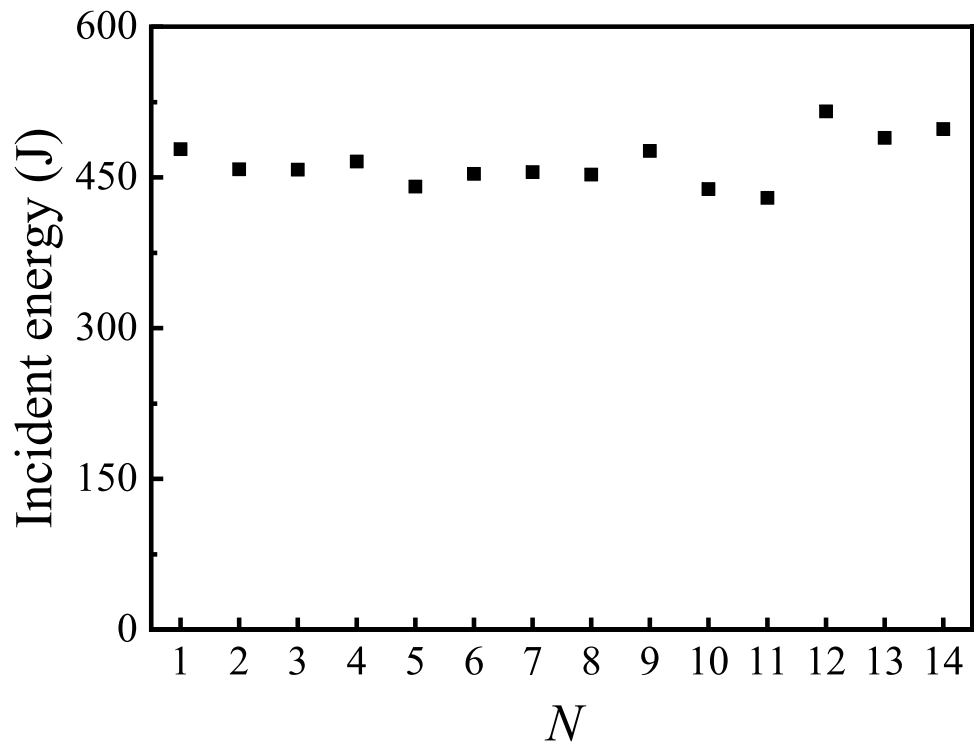
under hydrostatic pressure of 15 MPa. The differential pore pressure should be lower than the hydrostatic pressure and was set as 1 MPa, 3 MPa, 5 MPa, 7 MPa, 9 MPa, 11 MPa, and 13 MPa, respectively. The same air pressure was used to launch the striker for each impact and a C1100 copper disc with a diameter of 9 mm and a thickness of 1.5 mm was selected as the pulse shaper [34] for each impact. In this way, the incident energy for each impact can be precisely controlled at a relatively constant value. Based on one-dimensional stress wave theory, the incident energy is calculated by

$$W_i = \int_0^{T_0} EA c_0 \epsilon_i^2 d\tau \tag{8}$$

where  $E$  and  $A$  are the elastic modulus and cross-sectional area of bars,  $c_0$  is the longitudinal wave velocity of the bar,  $\epsilon_i$  is the incident strain wave,  $T_0$  is the duration of the incident wave. The incident energy for each impact in a typical cyclic impact experiment is shown in Fig. 7. It is clear that the incident energy for each impact is almost constant, indicating that the constant incident energy in each cycle can be achieved successfully using the same impact velocity of the striker.

The dynamic stress–strain curves of GS under cyclic impacts with constant input energy are shown in Fig. 8. The stress–strain curves undergo significant changes as the increase of impact number. Between the 1st and 3rd impact cycles, there are obvious concave segments on the stress–strain curve at the initial compaction stage.

Fig. 7 Incident energy for each impact in a typical dynamic experiment



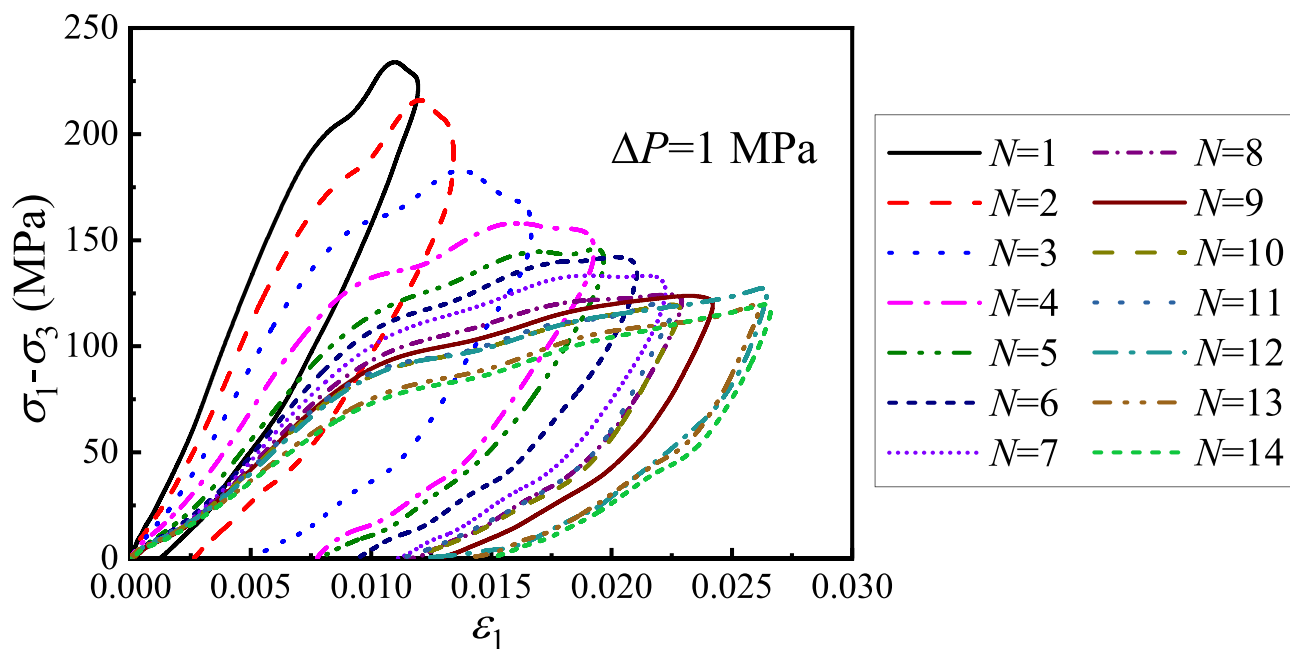


**Fig. 8** Dynamic stress–strain curves after cyclic impacts with constant incident energy in a typical experiment

Subsequently, there is a stage of linear elastic deformation, where the stress–strain curve grows approximately linearly and the slope of the curve is precipitous. Thereafter, the stress–strain curves deviate from linear growth, exhibiting an upward convex trend and reaching the peak stress during the plastic deformation stage. This stage is relatively short, indicating minimal damage to the GS specimen. Finally, in the unloading stage after the stress peak, the stress and strain decrease until the stress reaches zero, while a small residual strain remains. The unloading curve has a similar slope to the loading curve, suggesting that the damage caused by the input energy is minimal. Most of the energy is stored in the specimen in the form of elastic strain energy and is released during the unloading stage, resulting in a hysteresis loop in the post-peak unloading segment. Moreover, between the 4th and 7th impact cycles, there is a small "stress plateau" that appeared at the peak stress stage. As the number of impacts increases, the dynamic elastic modulus of the specimen decreases significantly, the peak stress decreases apparently, and the residual deformation increases. Although after the peak stress the damage was induced inside the specimen, the damaged specimen was tightly bound and still able to withstand a certain load under the constraint of confining pressure. These mechanical properties exhibit a noticeable trend of damage during this loading period. Furthermore, between the 8th and 14th impact cycles, the stress–strain curve is similar to that of the seventh impact, indicating that the GS specimen was basically in a completely damaged state after the seventh impact.

Figure 9 illustrates the variation of dynamic compressive strength with the number of impacts with the constant incident energy. Between the 1st and 7th impact cycles, the dynamic compressive strength decreases rapidly with the increase of impact number. Between the 8th and 14th impact cycles, the dynamic compressive strength decreases slowly with the increase of impact number, indicating that the rock specimen is gradually damaged after the 8th impact cycle. In addition, it can be found that the differential pore pressure has a significant effect on the dynamic compressive strength of GS. With the increase of the differential pore pressure, the overall trend of the peak stress with the number of impacts alters downward, demonstrating a substantial reduction in the peak stress [35]. This can be explained by two aspects: a) The mean effective stress of the GS specimen decreases with increasing upstream pore pressure, which would contribute to the decrease of the dynamic compressive strength of the GS specimen; b) The presence of a permeation gradient within the GS specimen at the differential pore pressure, which promotes crack propagation and increases the damage, thus reducing the strength of GS. Moreover, the presence of internal pore pressure counteracts the contact force between particles, leading to particle separation and the increase of specimen damage, further lowering the dynamic compressive strength. Meanwhile, the existence of the differential pore pressure offsets part of the confining pressure, reducing the constraining effect of effective confining pressure on the specimen and consequently lowering the dynamic compressive strength based on the principle of effective stress.

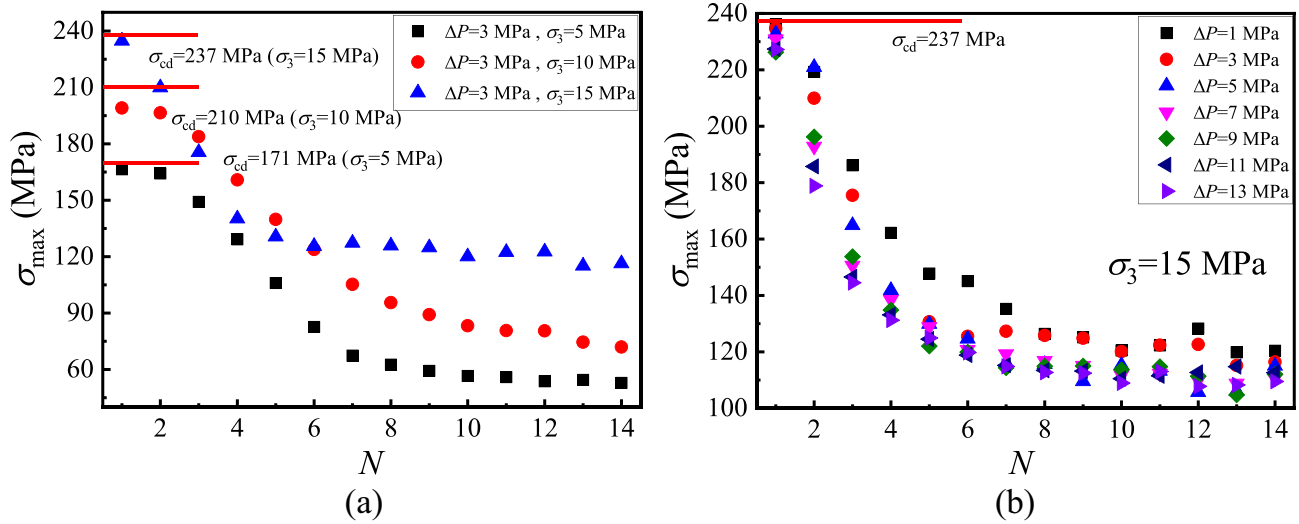


**Fig. 9** Evolution of dynamic compressive strength of GS after cyclic impacts with constant input energy under (a) various confining pressures and (b) various differential pore pressures (Note: the red line is the dynamic compressive strength of GS under a certain incident energy.)

**Evolution of Permeability of Rocks Under Cyclic Impacts**

Figure 10 shows the permeability evolution of GS with the impact number. Figure 10a indicates that the permeability of GS under the same differential pore pressure and impact cycle is significantly affected by the confining pressure. Meanwhile, based on the experimental results on various confining pressures and differential pore pressures in Fig. 10, the repeatability of the testing system in this study is proved. As shown in Fig. 10b, From the 1st to 3rd impact cycles, the permeability of GS gradually increases with the

increase of impact number. At this stage, new cracks are generated inside the GS specimen, but the cracks are not yet coalesced during the first three impact cycles, and the damage level of the GS specimen varies slightly. Additionally, from the 4th to 7th impact cycles, the permeability of GS increases rapidly with the impact number, and the peak permeability of GS is reached after the seventh impact. The reason for this phenomenon is that the subsequent impacts generate more new cracks inside the specimen, increasing areas of crack surfaces and intensifying connections among cracks. Eventually, a great number of wide and continuous flow channels were formed within the GS specimen,

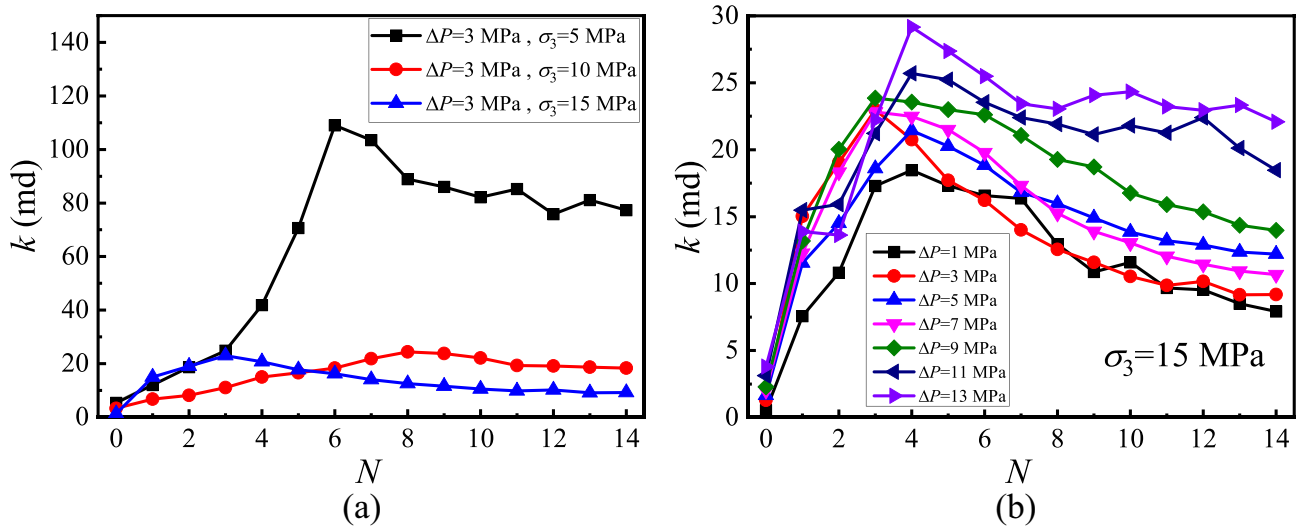


**Fig. 10** Evolution of permeability of rock specimens after cyclic impacts with constant input energy under (a) various confining pressures and (b) various differential pore pressures

leading to an obvious increase in permeability and reaching the peak permeability. Furthermore, from the 8th to 14th impact cycles, the permeability slowly decreases with the increase of impact number. This is attributed to the formation of shear fracture zones, where small fragments move along macroscopic fracture surfaces. In shear fracture zones, a large number of fine particles may be generated, which may move along the seepage channel and produce blockage due to the seepage gradient [36, 37]. Thus, the blockage of the seepage channel decreases the permeability of the GS specimen. Meanwhile, the shear fracture zones are tightly compacted by the confining pressure, resulting in a decrease in channel aperture and further a decrease in permeability.

As shown in Fig. 10b, it can also be observed that the differential pore pressure has an apparent impact on permeability. The permeability increases with the increase of the differential pore pressure under the constant confining pressure. On the one hand, the differential pore pressure and the seepage gradient within the specimen contribute to the expansion and development of cracks, increasing the number of cracks, the growth in crack length, and the coalescence of cracks. On the other hand, high differential pore pressure can enlarge the aperture of the flow channels, thereby increasing the permeability [38, 39].

## Failure Mode of Rocks Under Cyclic Impacts

To investigate the effects of cyclic impacts and differential pore pressures on the development of crack networks, all specimens were recovered after impact experiments, and the images of three-dimensional crack distribution under different differential pore pressures were obtained using the micro-CT system (Nano Voxel X-Ray 3D Microscope System), as shown in Fig. 11. It can be seen that the small cracks surround the perimeter of the specimen, and the main cracks develop along a certain angle with the loading direction (i.e., perpendicular to two ends of the cylinder specimen). The main cracks, which have acute angles with the loading direction, are formed an hourglass in the GS specimens, indicating that the main cracks present a conjugate shear crack morphology observed from the side direction and the macroscopic failure mode of the GS specimen is mainly compression shear failure. This failure mode is similar to the recovered specimens subjected to the dynamic compressive loading and the static triaxial stress using the triaxial SHPB experiments [4, 14]. It can be seen from Fig. 11 that with the increase of the differential pore pressure, the contour of hourglass cracks in the GS specimen becomes more and more clear and complete, and finally cracks through the specimen are formed. This demonstrates that the differential pore pressure

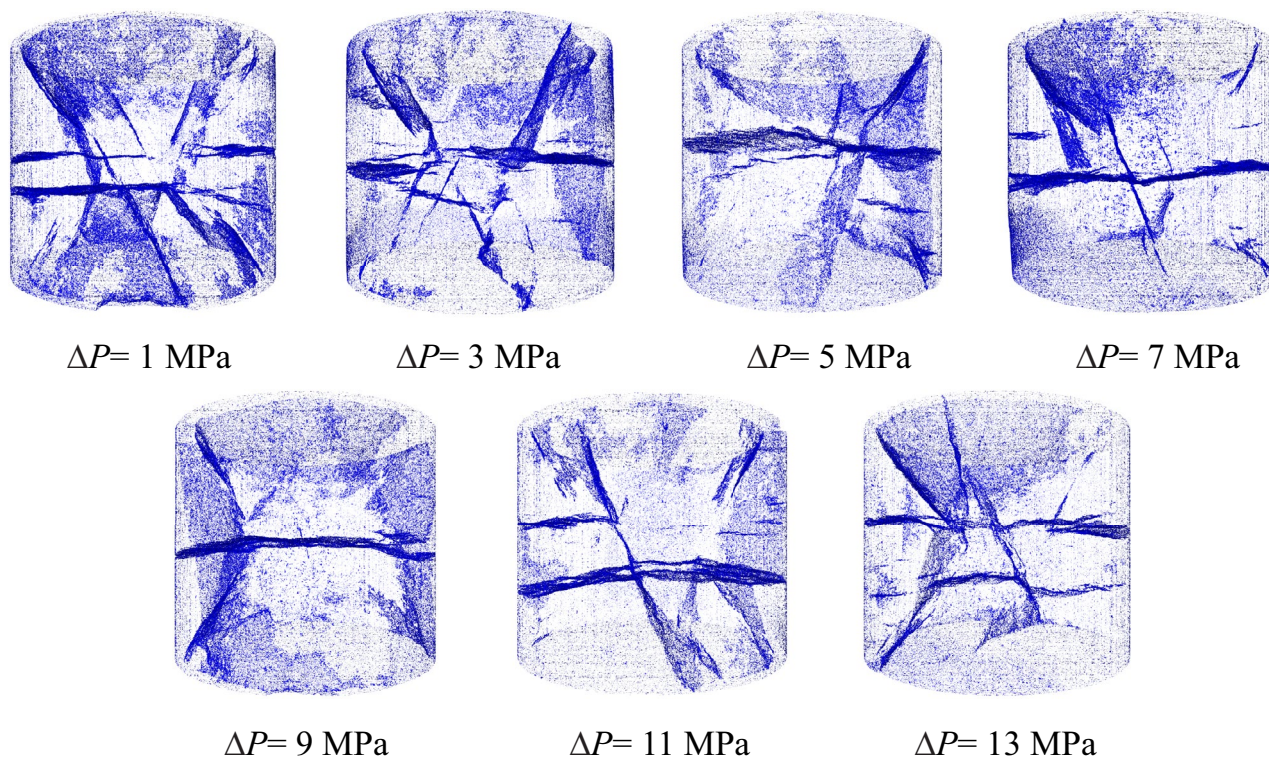


Fig. 11 Crack distribution in recovered specimens under different differential pore pressures after cyclic impacts with constant input energy

is conducive to crack growth from a microscopic perspective, which also reveals the reason why the permeability gradually increases with the increase of the differential pore pressure. Another important finding is that a macroscopic tensile crack can also be found in the middle of the GS specimen, which may be caused by the coupling effect of reflection waves in the specimen, the differential pore pressure, and the confining pressure. In our previous study, after the dynamic loading condition, this tensile failure can also be observed in the rock specimen under the hydrostatic pressure and the pore pressure [14]. This means that this tensile fracture is mainly caused by the coupling effect of the pore pressure and the confining pressure. It is difficult to determine if the tensile fracture occurs after shear fractures. However, in most cases, the shear fracture passes generally through the tensile fracture just as there is no tensile fracture, indicating that the rock specimen can be considered as a whole cylinder when the shear fracture is generated. Consequently, the dynamic compressive strength obtained in this testing system is valid. In summary, the characteristics of crack distribution for various differential pore pressures are subtly different, reflecting the influence of the differential pore pressure on the damage and permeability evolution of the GS specimen.

## Conclusions

In this study, the triaxial dynamic rock testing apparatus with the differential pore pressure system was developed to provide a novel method for evaluating the effect of differential pore pressure on the dynamic mechanical properties and permeability evolution of rocks under different differential pore pressures, different confining pressures, and different strain rates. The proposed system is mainly composed of a conventional SHPB system, an in-situ stress system, a differential pore pressure system, and a data acquisition system. The applicability and flexibility of this system are verified through dynamic compressive tests using the GS specimen under cyclic impacts under various differential pore pressures. The dynamic compressive strength and the permeability evolution of the GS specimen under cyclic impacts with constant input energy and different differential pore pressures were measured, and the influence of the differential pore pressure on the damage and permeability evolution of GS was explored. The main conclusions are drawn as follows:

1. The stress–strain curve shows an obvious deterioration trend with the increase of impact number before the seventh impact, and there is no significant change in the stress–strain curve after the eighth impact. This phenomenon indicates that the GS specimen was basically in a completely damaged state after the seventh impact. In addition, the dynamic compressive strength of GS decreases rapidly with the increase of the impact number before the seventh impact, and then slowly decreases or remains almost stable after the seventh impact. The dynamic compressive strength of GS decreases with the increase of the differential pore pressure.
2. The permeability of GS under the same impact number increases with the increase of the differential pore pressure and decreases with the confining pressure. From the 1st to 3rd impact cycles, the permeability of GS gradually increases with the increase of impact number. From the 4th to 7th impact cycles, the permeability of GS increases rapidly with the impact number, and the peak permeability of GS is reached after the seventh impact. From the 8th to 14th impact cycles, the permeability slowly decreases with the increase of impact number.
3. The CT images of recovered specimens show that the small cracks surround the perimeter of the specimen and the main cracks develop along a certain angle with the loading direction. The main cracks present a conjugate shear crack morphology observed from the side direction and the macroscopic failure mode of the GS specimen is mainly compression shear failure. Another important finding is that a macroscopic tensile crack can also be found in the middle of the GS specimen, which may be caused by the coupling effect of reflection waves in the specimen, the differential pore pressure, and the confining pressure. Differential pore pressure has a significant deterioration mechanism on the mechanical properties of deep rock mass, which can promote the development of rock fractures and increase the permeability of rocks.

**Supplementary Information** The online version contains supplementary material available at <https://doi.org/10.1007/s11340-024-01063-z>.

**Acknowledgements** This work was supported by the National Natural Science Foundation of China (Grant Nos. 42141010, 12172253, and 12072369) and the Natural Science Foundation of Hunan Province (2022JJ10058).

**Author Contributions** Conceptualization: Kaiwen Xia, Wei Yao; Methodology: Kaiwen Xia, Wei Yao, Geli Zhao, Rong Chen; Formal analysis and investigation: Rong Chen, Geli Zhao, Ying Xu, Weili Yao, Kaiwen Xia; Writing—original draft preparation: Wei Yao, Rong Chen, Geli Zhao; Writing—review and editing: Rong Chen, Wei Yao, Geli Zhao, Ying Xu, Weili Yao; Funding acquisition: Kaiwen Xia, Ying Xu, Wei Yao; Resources: Kaiwen Xia, Wei Yao.

**Data Availability** The related data used to support the findings of this study are included within the article and are available from the corresponding author upon reasonable request.

## Declarations

**Competing Interest** The authors declare that they have no known competing financial interests or personal relationships that could have appeared to influence the work reported in this paper.

## References

- Zhang Q, Zhao J (2014) A Review of Dynamic Experimental Techniques and Mechanical Behaviour of Rock Materials. *Rock Mech Rock Eng* 47:1411–1478. <https://doi.org/10.1007/s00603-013-0463-y>
- Wagner H (2019) Deep Mining: A Rock Engineering Challenge. *Rock Mech Rock Eng* 52(5):1417–1446. <https://doi.org/10.1007/s00603-019-01799-4>
- Ranjith PG, Zhao J, Ju MH, De Silva RVS, Rathnaweera TD, Bandara A (2017) Opportunities and Challenges in Deep Mining: A Brief Review. *Engineering* 3(4):546–551. <https://doi.org/10.1016/j.eng.2017.04.024>
- Gong FQ, Si XF, Li XB, Wang SY (2019) Dynamic triaxial compression tests on sandstone at high strain rates and low confining pressures with split Hopkinson pressure bar. *Int J Rock Mech Min Sci* 113:211–219. <https://doi.org/10.1016/j.ijrmms.2018.12.005>
- Zhou Z, Cai X, Ma D, Du X, Chen L, Wang H, Zang H (2019) Water saturation effects on dynamic fracture behavior of sandstone. *Int J Rock Mech Min Sci* 114:46–61. <https://doi.org/10.1016/j.ijrmms.2018.12.014>
- Wang H, Jin W, Li Q (2009) Saturation Effect on Dynamic Tensile and Compressive Strength of Concrete. *Adv Struct Eng* 12(2):279–286. <https://doi.org/10.1260/136943309788251713>
- Zheng D, Li Q (2004) An explanation for rate effect of concrete strength based on fracture toughness including free water viscosity. *Eng Fract Mech* 71(16):2319–2327. <https://doi.org/10.1016/j.engfracmech.2004.01.012>
- Lu A, Hu S, Li M, Duan T, Li B, Chang X (2019) Impact of Moisture Content on the Dynamic Failure Energy Dissipation Characteristics of Sandstone. *Shock Vib* 2019:1–10. <https://doi.org/10.1155/2019/6078342>
- Cai X, Zhou Z, Zang H, Song Z (2020) Water saturation effects on dynamic behavior and microstructure damage of sandstone: Phenomena and mechanisms. *Eng Geol* 276:105760. <https://doi.org/10.1016/j.enggeo.2020.105760>
- Cai X, Zhou Z, Du X (2020) Water-induced variations in dynamic behavior and failure characteristics of sandstone subjected to simulated geo-stress. *Int J Rock Mech Min Sci* 130:104339. <https://doi.org/10.1016/j.ijrmms.2020.104339>
- Zhou Z-l, Cai X, Zhao Y, Chen L, Xiong C, Li X-b (2016) Strength characteristics of dry and saturated rock at different strain rates. *Trans Nonferrous Metals Soc China* 26(7):1919–1925. [https://doi.org/10.1016/S1003-6326\(16\)64314-5](https://doi.org/10.1016/S1003-6326(16)64314-5)
- Zhou Z-h, Cao P, Ye Z-y (2014) Crack propagation mechanism of compression-shear rock under static-dynamic loading and seepage water pressure. *J Central South Univ* 21(4):1565–1570. <https://doi.org/10.1007/s11771-014-2097-y>
- Wang K, Feng G, Bai J, Guo J, Shi X, Cui B, Song C (2022) Dynamic behaviour and failure mechanism of coal subjected to coupled water-static-dynamic loads. *Soil Dyn Earthq Eng* 153:107084. <https://doi.org/10.1016/j.soildyn.2021.107084>
- Zhao G, Li X, Xu Y, Xia K (2022) A modified triaxial split Hopkinson pressure bar (SHPB) system for quantifying the dynamic compressive response of porous rocks subjected to coupled hydraulic-mechanical loading. *Geomech Geophys Geo-Energy Geo-Resour* 8(1):29. <https://doi.org/10.1007/s40948-021-00335-5>
- Liu C, Deng H, Wang Y, Lin Y, Zhao H (2017) Time-varying characteristics of granite microstructures after cyclic dynamic disturbance using nuclear magnetic resonance. *Crystals* 7(10):306
- Yan L, Yi W, Liu L, Liu J, Zhang S (2018) Blasting-induced permeability enhancement of ore deposits associated with low-permeability weakly weathered granites based on the split hopkinson pressure bar. *Geofluids* 2018:4267878. <https://doi.org/10.1155/2018/4267878>
- Jiang Z, Yu S, Deng H, Deng J, Zhou K (2019) Investigation on microstructure and damage of sandstone under cyclic dynamic impact. *IEEE Access* 7:133145–133158. <https://doi.org/10.1109/ACCESS.2019.2929234>
- Wang S, Xu Y, Xia K, Tong T (2021) Dynamic fragmentation of microwave irradiated rock. *J Rock Mech Geotech Eng* 13(2):300–310. <https://doi.org/10.1016/j.jrmge.2020.09.003>
- Xia K, Yao W (2015) Dynamic rock tests using split Hopkinson (Kolsky) bar system – A review. *J Rock Mech Geotech Eng* 7(1):27–59. <https://doi.org/10.1016/j.jrmge.2014.07.008>
- Song B, Chen W (2004) Loading and unloading split hopkinson pressure bar pulse-shaping techniques for dynamic hysteretic loops. *Exp Mech* 44(6):622–627. <https://doi.org/10.1007/BF02428252>
- Nemat-Nasser S, Isaacs J, Starrett J (1991) Hopkinson techniques for dynamic recovery experiments. *Proc Royal Soc A: Math Phys Eng Sci* 435:371–391. <https://doi.org/10.1098/rspa.1991.0150>
- Xia K, Wang S, Xu Y, Chen R, Wu B (2021) Advances in experimental studies for deep rock dynamics. *Chin J Rock Mech Eng* 40:448–475. <https://doi.org/10.13722/j.cnki.jrme.2020.0343>
- Ulusay R (2015) The ISRM Suggested Methods for Rock Characterization, Testing and Monitoring 2007–2014. <https://doi.org/10.1007/978-3-319-07713-0>
- Zhou YX, Xia K, Li XB, Li HB, Ma GW, Zhao J, Zhou ZL, Dai F (2012) Suggested methods for determining the dynamic strength parameters and mode-I fracture toughness of rock materials. *Int J Rock Mech Min Sci* 49:105–112. <https://doi.org/10.1016/j.ijrmms.2011.10.004>
- Xu Y, Yao W, Xia K, Ghaffari HO (2019) Experimental Study of the Dynamic Shear Response of Rocks Using a Modified Punch Shear Method. *Rock Mech Rock Eng* 52(8):2523–2534. <https://doi.org/10.1007/s00603-019-1744-x>
- Du H-b, Dai F, Liu Y, Xu Y, Wei M-d (2020) Dynamic response and failure mechanism of hydrostatically pressurized rocks subjected to high loading rate impacting. *Soil Dyn Earthq Eng* 129:105927. <https://doi.org/10.1016/j.soildyn.2019.105927>
- Hokka M, Black J, Tkalic D, Fourmeau M, Kane A, Hoang NH, Li CC, Chen WW, Kuokkala VT (2016) Effects of strain rate and confining pressure on the compressive behavior of Kuru granite. *Int J Impact Eng* 91:183–193. <https://doi.org/10.1016/j.ijimpeng.2016.01.010>
- Hopkinson B (1914) A Method of Measuring the Pressure Produced in the Detonation of High Explosives or by the Impact of Bullets. *Philos Trans Royal Soc London Series A, Containing Papers Math Phys Char* 213:437–456. <https://doi.org/10.1098/rsta.1914.0010>
- Davies RM, Taylor GI (1997) A critical study of the Hopkinson pressure bar. *Philos Trans Royal Soc London Series A, Math Phys Sci* 240(821):375–457. <https://doi.org/10.1098/rsta.1948.0001>
- Kolsky H (1949) An Investigation of the Mechanical Properties of Materials at very High Rates of Loading. *Proc Phys Soc London, Sect B* 62(11):676. <https://doi.org/10.1088/0370-1301/62/11/302>
- Lu A, Hu S, Li M, Duan T, Li B, Chang X (2019) Impact of moisture content on the dynamic failure energy dissipation characteristics of sandstone. *Shock Vib* 2019:6078342. <https://doi.org/10.1155/2019/6078342>
- Kruczek B (2015) Carman–Kozeny equation. *encyclopedia of membranes*. Springer Berlin Heidelberg, Berlin, Heidelberg. [https://doi.org/10.1007/978-3-642-40872-4\\_1995-1](https://doi.org/10.1007/978-3-642-40872-4_1995-1)
- Sander R, Pan Z, Connell LD (2017) Laboratory measurement of low permeability unconventional gas reservoir rocks: A review of experimental methods. *J Nat Gas Sci Eng* 37:248–279. <https://doi.org/10.1016/j.jngse.2016.11.041>
- Frew DJ, Forrestal MJ, Chen W (2002) Pulse shaping techniques for testing brittle materials with a split hopkinson pressure bar. *Exp Mech* 42(1):93–106. <https://doi.org/10.1007/BF02411056>
- Xiao W, Zhang D, Wang X (2020) Experimental study on progressive failure process and permeability characteristics of red



- sandstone under seepage pressure. *Eng Geol* 265:105406. <https://doi.org/10.1016/j.enggeo.2019.105406>
36. David C, Menendez B, Zhu W, Tf W (2001) Mechanical compaction, microstructures and permeability evolution in sandstones. *Phys Chem Earth Part A* 26(1):45–51. [https://doi.org/10.1016/S1464-1895\(01\)00021-7](https://doi.org/10.1016/S1464-1895(01)00021-7)
37. Heiland J, Raab S (2001) Experimental investigation of the influence of differential stress on permeability of a lower permian (rotliegend) sandstone deformed in the brittle deformation field. *Phys Chem Earth Part A* 26(1):33–38. [https://doi.org/10.1016/S1464-1895\(01\)00019-9](https://doi.org/10.1016/S1464-1895(01)00019-9)
38. Li M, Liu X (2021) Experimental and numerical investigation of the failure mechanism and permeability evolution of sandstone based on hydro-mechanical coupling. *J Nat Gas Sci Eng* 95:104240. <https://doi.org/10.1016/j.jngse.2021.104240>
39. Chen X, Yu J, Ca T, Li H, Wang S (2017) Experimental and numerical investigation of permeability evolution with damage of sandstone under triaxial compression. *Rock Mech Rock Eng* 50(6):1529–1549. <https://doi.org/10.1007/s00603-017-1169-3>

**Publisher's Note** Springer Nature remains neutral with regard to jurisdictional claims in published maps and institutional affiliations.

Springer Nature or its licensor (e.g. a society or other partner) holds exclusive rights to this article under a publishing agreement with the author(s) or other rightsholder(s); author self-archiving of the accepted manuscript version of this article is solely governed by the terms of such publishing agreement and applicable law.